ChemComm

COMMUNICATION

View Article Online
View Journal | View Issue

Cite this: *Chem. Commun.*, 2026, **62**, 2957

Received 20th September 2025,
Accepted 5th January 2026

DOI: 10.1039/d5cc05420f

rsc.li/chemcomm

Fe single-atom catalysts supported on N-enriched carbon promote the liquid phase electro-reduction of carbon dioxide to formic acid

Gema Martinez,†[abcd] Stefan Delgado,†[e] Ainhoa Madrid,[ac] Sergio Díaz-Coello,[e] Ekaterina Pakrieva,[abc] María del Carmen Arévalo,[e] Elena Pastor,*[e] Jose L. Hueso*[abcfg] and Jesus Santamaria[abcf]

This work describes how the presence of Fe single atom catalysts (Fe-SAC) dispersed on a nitrogen-enriched carbon matrix favours the selective electrocatalytic reduction of dissolved carbon dioxide to formic acid in neutral medium. Fe-SAC and Fe-free carbons were prepared by laser pyrolysis of phthalocyanine-pyridine aerosols.

Carbon dioxide conversion into added-value chemicals and fuels represents a formidable challenge towards a sustainable energy transition. Current innovation and research strategies include: (i) novel process intensification reactors with alternative activation strategies (*i.e.* photons, plasma, microwaves, electricity)[1–7] and (ii) the development of innovative materials able to maximize the interaction (adsorption–reaction) with CO_2. Regarding the latter, the use of atomically dispersed catalysts (also known as single-atom catalysts or SACs) emerges as one of the most promising strategies to achieve highly selective conversion of CO_2 while minimizing the use of expensive and scarce noble metals.[8–15] The combination of transition metal based SACs (*i.e.* Cu, Co, Fe) and electrocatalysis has yielded excellent results to obtain highly selective conversion of CO_2 into light hydrocarbons or alcohols, although there is still room to improve the interaction of dissolved CO_2 with the catalysts.[2,16–20] Some of the most successful SACs for CO_2 reduction are based on isolated atoms dispersed in carbon matrices generally obtained by top-down thermal decomposition of preformed metal–organic frameworks (MOFs). This yields a high control on the catalyst structure key for some designs (*e.g.* dual-metal SACs) and benefits from the high conductivity of the carbon matrix obtained.[10,21–24] However, it also increases complexity, as it involves an additional synthesis step, and cost (the use of an expensive MOF material as a sacrificial matrix). In this work, we used a direct bottom-up approach based on the laser-driven pyrolysis of aerosols containing Fe-phthalocyanine (Fe-Ph) suspended in pyridine to obtain Fe-SACs supported within a carbon matrix (Fig. 1a and Fig. S1). The continuous wave infrared laser instantly decomposes the precursor droplets thereby trapping the isolated metals in a carbon matrix and minimizing nanoparticle nucleation and growth events during the decomposition process.[25] In addition, a rapid quenching occurs out of the laser reaction zone (a temperature decrease of up to 150 degrees per mm)[26] also preventing migration and coalescence of atoms. We also synthesized Fe-free N-doped carbons under analogous reaction conditions with Fe-free Ph to yield N-enriched carbons (Fe-free N-Cs) (Fig. S2) and establish the influence of the Fe sites on the electrocatalytic reduction of CO_2 (ECO_2RR).

Fig. 1b–d and Fig. S1 show evidence of atomically dispersed Fe features in N-doped carbons. Additional evidence from EXAFS data was presented in previous works.[24] The carbon particles hold an uneven size distribution and exhibit partial interconnection as previously observed in other particle morphologies synthesized by laser pyrolysis. The brighter contrast spots correspond to the presence of atomically dispersed Fe atoms with higher Z number. Overall, the EDX signal of Fe could only be detected after accumulation in broad areas (Fig. S3). Furthermore, N signal could be also detected for both the Fe-SACs and specially its Fe-free N-Cs counterpart (Fig. S2c). The N_2 adsorption–desorption isotherms showed a slight separation between the adsorption and desorption branches at higher relative pressures ($p/p^0 > 0.8$), suggesting the

[a] *Instituto de Nanociencia y Materiales de Aragon (INMA) CSIC-Universidad de Zaragoza, Campus Rio Ebro, Edificio I + D, C/Poeta Mariano Esquillor, s/n, 50018, Zaragoza, Spain. E-mail: jlhueso@unizar.es*
[b] *Department of Chemical and Environmental Engineering, University of Zaragoza, Campus Rio Ebro, C/María de Luna, 3, 50018 Zaragoza, Spain*
[c] *Networking Research Center on Bioengineering, Biomaterials and Nanomedicine (CIBER-BBN), 28029, Madrid, Spain*
[d] *Centro Universitario de la Defensa (CUD), Ctra. de Huesca, 50090 Zaragoza, Spain*
[e] *Instituto de Materiales y Nanotecnología, Departamento de Química, Universidad de La Laguna, Av. Astrofísico Francisco Sánchez s/n, 38206, San Cristóbal de La Laguna, España. E-mail: epastor@ull.edu.es*
[f] *Instituto de Investigación Sanitaria (IIS) de Aragón, Avenida San Juan Bosco, 1350009 Zaragoza, Spain*
[g] *Escuela Politécnica Superior, U. Zaragoza, Crta. de Cuarte s/n 22071, Huesca, Spain*
† Equal contribution.

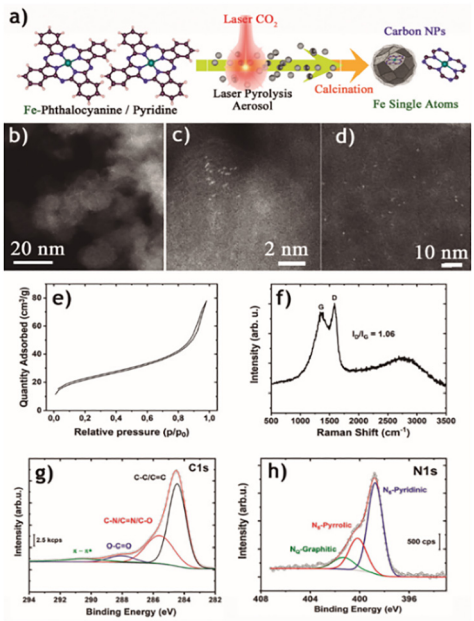

Fig. 1 Synthesis and characterization of Fe-SAC by laser pyrolysis: (a) simplified scheme of laser driven pyrolysis of Fe-phthalocyanine-pyridine aerosol droplets to yield Fe-SACs. (b–d) HAADF-STEM representative images of the Fe-SACs samples; (e) N_2 adsorption isotherms at 77 K of the Fe-SACs; (f) representative Raman spectrum of the Fe-SACs; (g) fitted XPS of the C 1s region; (h) fitted XPS of the N 1s region.

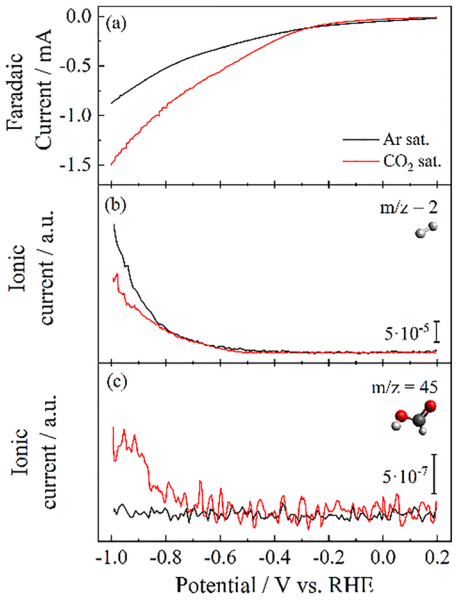

Fig. 2 LSVs (a) and the corresponding MSLSVs for m/z = 2 (b), m/z = 45 (c), recorded for Fe-SAC in 0.1 M phosphate buffer solution (pH = 7.5) at 2 mV s^{-1}, in Argon and CO_2 saturated solutions, respectively.

presence of mesopores but with only a minor hysteresis loop (Fig. 1e and Fig. S2e).

Given the limited Fe content, partial pore blockage can be ruled out, and a change of chemical properties due to structural rearrangements caused by metal coordination seems a more likely cause. The pore size distributions, calculated using the non-local density functional theory (NLDFT) method, confirm that both materials possess pores within the mesoporous range (2–13 nm) (Fig. S4). The Fe-free N-Cs featured a broader mesoporous distribution, along with a total pore volume of 0.24 cm^3 g^{-1}, whereas the Fe-SAC exhibited substantially lower porosity (0.12 cm^3 g^{-1}), indicating that the presence of Fe effectively produces a denser material (Table S1). Raman analysis confirmed the presence of both disordered and graphitic domains at ~1350 cm^{-1} and ~1590 cm^{-1}, respectively (Fig. 1f and Fig. S2f). The higher I_D/I_G ratio for the Fe-SAC further suggested a higher disorder state induced by the presence of isolated Fe. X-ray photoelectron spectroscopy (XPS) revealed the surface composition for both samples with significant presence of C, N and O and trace signals of S or F (from SF_6, employed as a sensitizer). Fe signal was barely detectable for Fe-SAC (Fig. S5 and Table S2). Fitting of the C 1s region revealed the presence of C–N/C–O species at B.E.s of 286.5 eV, O–C=O species at 287.9 eV and π–π* interactions at 290 eV, respectively (Fig. 1g and Fig. S2g). Likewise, the fitting of the N 1s region[27] revealed the presence of pyridinic-N (B.E. = 398.3 eV), pyrrolic-N (400.1 eV), quaternary-N (401.5 eV) in both samples, along with the additional appearance of oxidized-N in the Fe-free N-C above 403 eV confirming the presence of N-enriched domains formed by laser pyrolysis (Fig. S1h). The catalytic response of Fe-SAC was evaluated towards the ECO_2RR in neutral medium (phosphate buffer solution; pH = 7.4) using Differential Electrochemical Mass Spectrometry (DEMS)[28] to simultaneously monitor the faradaic current and the ionic currents associated with the reaction products (see Note S1, Fig. 2 and Fig. S6–S8). Briefly, the experiment was carried out in a three-electrode half-cell where a glassy carbon disk was modified with 20 μL of the catalytic ink and used as working electrode. The amount of ink was set to obtain a metallic load of 0.09 μg of Fe. The electrode was immersed at 0.2 V in a buffer phosphate solution (0.1 M Na_2HPO_4/0.1 M $NaH_2PO_4{\cdot}2H_2O$; pH = 7.5) saturated with CO_2 (99.998%). Then, the surface potential was linearly swept towards cathodic values while recording both the faradaic current and the respective ionic currents (see the Experimental methods in the SI for further details). A control experiment in Ar ambient (in absence of CO_2) was also carried out for comparison. Fig. 2a shows that the saturation of the electrolyte with CO_2 increased the faradaic response during the cathodic polarization (linear sweep voltammetry, LSV) of the catalyst. In particular, the total current at −1.0 V increases from −0.8 mA to −1.5 mA, revealing the existence of an additional process corresponding to the ECO_2RR. This aligns well with the works reported by Varela *et al.*[29,30] On the other hand, Fig. 2b and c display the mass spectrometry signals (MSLSVs) corresponding to the evolution of hydrogen (m/z = 2) and formate (m/z = 45), respectively. While linking the m/z = 2 signal with the $[H_2]^+$ ion is straightforward, the correspondence of m/z = 45 with the $[HCOO]^+$ fragment from formate was established from the conditions of the experiment. Note S1 and Fig. S6 further explain about the most plausible product distribution and the species ruled out according to DEMS experiments. It is interesting to note that the

responses for m/z = 2 were practically identical in the presence and absence of CO_2 beyond the onset overpotential (approx. −0.5 V) until −0.8 V, but then the production of H_2 was lower for the CO_2 saturated solution. This indicates that the hydrogen evolution reaction (HER) is partially blocked during the ECO_2RR (Scheme S1). No additional by-products associated with the ECO_2RR were identified by DEMS (*e.g.*, methane monitored by the signal m/z = 15, Fig. S7b, or methanol by the mass m/z = 31, Fig. S8d). This is important since it contrasts with the high efficiency towards methane reported for other Fe-based materials.[30]

At −0.5 V the signal for m/z = 45 started being detected, revealing the formation of formate as the main product of the ECO_2RR process (Fig. 2c). Hence, the Fe-SAC: (i) preferentially produces formic acid during the ECO_2RR in neutral medium (Scheme S1); and (ii) does not lead to the formation of C_2 products. The faradaic efficiencies (FE) towards the HER have been estimated by comparing the ionic currents before and after CO_2 saturation of the electrolyte (see Fig. S9). As no other products besides H_2 and formate were detected in the potential range between −0.65 and −0.90 V *vs.* RHE, we assume that the difference between FE for H_2 in CO_2-saturated conditions is due to the generation of formate. Thus, a FE of ∼57% at −0.90 V have been derived from the experiments. This agrees with the characteristics of SACs materials since each isolated Fe site acts as a center of reaction for the CO_2 molecule, sterically avoiding the C–C coupling of two different molecules.[18]

As shown in Table S3, analogous materials exhibit high selectivity towards the formation of CO due to the preferential adsorption of the CO_2 molecule to form the *COOH intermediate. In contrast, the laser pyrolysis method induces the generation of O-based functional groups, promoting instead the *OHCO adsorbate and formate formation (Note S2). As specified in the latter, as well as in Table S3, the selectivity towards formate was linked not only to the material itself, but also to the usage of pH = 5 phosphate buffer as electrolyte for the reaction. Finally, an increase in the signals for m/z = 32 and m/z = 28 was observed but these ionic currents are not related to other products of the ECO_2RR (see discussion below). In addition to the formation of formate as the main product of the ECO_2RR, DEMS also provided information about the mechanism from the Tafel slopes for H_2 production (Fig. 3 and Note S3). Indirectly, the evaluation of HER kinetics can shed light on the performance of the ECO_2RR since both reactions compete for the same active sites.[31–33] Typically, Tafel slopes are derived from LSV experiments. However, if the polarization response during the experiment does not exclusively arise from the HER, Tafel slope values are overestimated, as can be seen in Fig. 3a, with values that are clearly over the theoretical limit of 120 mV dec^{-1} (364 and 627 mV dec^{-1} respectively in the presence and absence of CO_2). Instead, we have used the method previously reported by Diaz-Coello *et al.*,[28,34] in which the Tafel slopes are derived for the HER from the m/z = 2 ionic currents recorded during the DEMS experiments. In this method, the linear regression of the slopes was calculated from the onset potential of the reaction (easily readable at the m/z = 2 panel of the DEMS experiment) and extended for 50 – 100 mV of the cathodic scan (if linearity is maintained in this range). Fig. S9

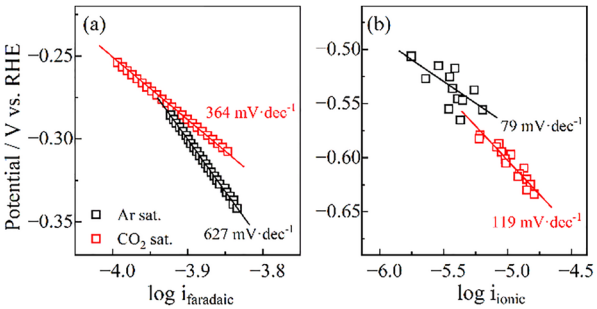

Fig. 3 Tafel plots derived from (a) faradaic currents and (b) m/z = 2 ionic currents recorded for Fe-SAC during the DEMS experiment shown in Fig. 2.

also marks the specific range used in this work, and Note S3 extends the information of the method and theory of the HER mechanism. Fig. 3b shows that this approximation resulted in Tafel slopes inside the range theoretically accepted (from 30 to 120 mV dec^{-1}). In the Ar saturated solution, a Tafel slope of 79 mV dec^{-1} was obtained, while in the CO_2 saturated electrolyte it shifted to 120 mV dec^{-1}. This implies a modification in the kinetics of HER. In the former reaction scenario, both the Volmer and the Heyrovsky reactions are involved in the rate-determining step (RDS) of the whole process.[34] Thus, some reaction sites are available to reduce water molecules, while others are kinetically hampered to facilitate the first reduction step of water.[32,33] In contrast, when the electrolyte is saturated with CO_2, the Tafel slope showed a value of 120 mV dec^{-1}, which implies the Volmer reaction as sole RDS of the process. This behavior suggests that CO_2 occupies active surface sites, thereby hindering H adsorption and inhibiting the HER. This is well aligned with the DEMS experiment presented on Fig. 2b, where the generation of H_2 significantly decreases. Additionally, the stability of Fe-SAC was studied by chronoamperometry (CA)-DEMS in the potential range of the HER. Fig. 4 shows an experiment carried out by recording the current transients at 0.2 V for 120 s, and then at −1.0 V for 300 s, respectively. Applying the latter potential to the material in the presence of CO_2 resulted in higher faradaic currents in comparison with the Ar saturated experiment (Fig. 4a) due to CO_2 electroreduction, confirming the results obtained in Fig. 2a. Furthermore, there was a significant inhibition in the formation of H_2 (m/z = 2, Fig. 4b) coupled with an enhanced formation of formate (m/z = 45, Fig. 4d) under CO_2 saturated conditions. This was also in agreement with the results presented in Fig. 2b and c. However, further screening of m/z from 15 to 32 values in DEMS experiments confirmed the sole presence of signals for m/z = 32 (Fig. 4c) and m/z = 28 (Fig. S7c and f) which led us to assign these mass ratios to $[N_2H_4]^+$ and $[N_2]^+$ fragments from the hydrazine molecule, respectively. The formation of hydrazine is obviously not arising from the reduction of CO_2, but rather as a product of the Fe center environment degradation, that is, hydrazine is produced from the N atoms anchoring the Fe to the C network. In the absence of CO_2, m/z = 32 (Fig. 4c, black line) increased after reaching −1.0 V and then it decreased over time, revealing the loss of active sites for hydrazine production under the applied potential. Remarkably, this process was accompanied by a

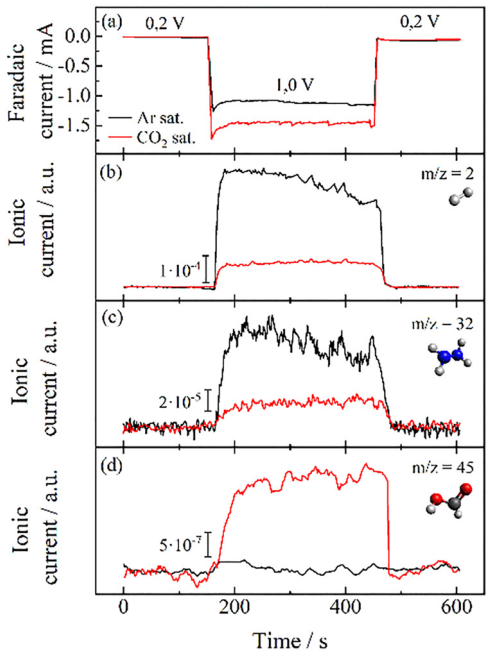

Fig. 4 (a) CA carried put in the presence and absence of CO_2 and corresponding mass spectra for: (b) m/z = 2, (c) m/z = 32 and, (d) m/z = 45 recorded over 10 minutes in 0.1 M phosphate buffer solution at pH 7.5.

decrease in the generation of H_2 (Fig. 4b, black line), which strengthens the hypothesis of the close correlation between both processes (Scheme S2). While hydrazine may hold certain safety concerns, in this study, our proposed degradation mechanism suggests the transformation of 1 mol of hydrazine per mol of Fe in the material (approx. 1.57×10^{-6} mol of Fe on top of the working electrode). Assuming complete degradation of the material, which was not the case, the amount of hydrazine generated would not reach the safety threshold. Remarkably, the DEMS experiment allowed the detection of this molecule, even at trace levels. Altogether, it seems reasonable that the hydrazine is formed by the hydrogenation of the N atoms in the Fe-based SAC due to the adsorption of H_2 at the Fe active centers (Scheme S2). However, this reaction was almost suppressed in the presence of dissolved CO_2 (Fig. 4c, red line) and the H adsorption step on the active site became the slowest process, and became impeded (Fig. 4b, red line), thereby increasing the stability and enabling the use of Fe-SAC for the ECO_2RR. To validate the specific influence of Fe to direct the selectivity towards hydrazine, we performed a control experiment with the Fe-free NCs (Fig. S10). This experiment was key to evaluate the behavior of the target material since no increase was found in m/z = 32 or 45 for the Fe-free carbon support. This demonstrated: (i) the catalytic activity of the metallic centers in the formation of formate; and (ii) the lack of formation of hydrazine in the absence of Fe. In both cases, the role of the Fe as reaction center was corroborated. This also confirmed that the active sites of the electrocatalyst are protected during the ECO_2RR. The stability towards the CO_2 reaction has also been tested (Fig. S11). The results show good stability under operating conditions for 1 hour with constant hydrogen and formate production. Remarkably, the same experiment in absence of CO_2 resulted in loss of activity caused by the degradation of the metallic center to form hydrazine after 45 min of applied potential (Fig. S11c). This confirms both the intrinsic stability of the material for the ECO_2RR reaction as well as the proposed mechanism for the degradation of the Fe center. In addition, the FE of the products have been calculated in this chronoamperometric experiment, showing approximately the same values as the polarization experiments in Fig. S9, corroborating the previous result. Summarizing, this work demonstrates the active role of Fe-SAC synthesized by laser pyrolysis to selectively electro-generate formate from CO_2 thereby paving the way towards the design of novel electrocatalysts based on Fe-SAC.

Conflicts of interest

There are no conflicts to declare.

Data availability

The data supporting this article have been included as part of the supplementary information (SI). Supplementary information: characterization techniques, additional figures and tables and experimental methods. See DOI: https://doi.org/10.1039/d5cc05420f.

Acknowledgements

The authors acknowledge funding from the Spanish Research Agency (AEI) through project CNS2022-135911 and Severo Ochoa: CEX2023-001286-S, Project PID2023-1507070B-I00, funded by MCIN/AEI/10.13039/501100011033, and the ULL-Cabildo de Tenerife-TALENTUM program. The synthesis of materials has been performed by the Platform of Production of Biomaterials and Nanoparticles of the NANBIOSIS ICTS, more specifically by the Nanoparticle Synthesis Unit (Unit 9) of the CIBER in Bioengineering, Biomaterials & Nanomedicine (CIBER-BBN). The authors acknowledge the use of instrumentation and technical support provided by the National Facility ELECMI ICTS, node 'Laboratorio de Microscopías Avanzadas (LMA)' at the Universidad de Zaragoza. S. D. thanks ACIISI (Agencia Canaria de Investigación, Innvovación y Sociedad de la Información) and the European Social Fund (ESF) (Operative Integrated Program of Canary Islands Integrated Operational Program 2021–2027, Area 3 Priority Theme 74 (85%)) for his predoctoral contract (TESIS2022010136). S. D-C. acknowledges the ULL-Cabildo de Tenerife-TALENTUM program for the postdoctoral contract. E. P. thanks Juan de la Cierva Formación postdoctoral fellowship (JDC2022-049007-I) financed by MICIU/AEI/10.13039/501100011033 and by the European Union "NextGenerationEU"/PRTR".

References

1 Y. Hori, K. Kikuchi and S. Suzuki, *Chem. Lett.*, 1985, **14**, 1695–1698.
2 S. Back, J. Lim, N.-Y. Kim, Y.-H. Kim and Y. Jung, *Chem. Sci.*, 2017, **8**, 1090–1096.
3 S. Nitopi, E. Bertheussen, S. B. Scott, X. Liu, A. K. Engstfeld, S. Horch, B. Seger, I. E. L. Stephens, K. Chan, C. Hahn, J. K. Nørskov, T. F. Jaramillo and I. Chorkendorff, *Chem. Rev.*, 2019, **119**, 7610–7672.
4 A. I. Stankiewicz and H. Nigar, *React. Chem. Eng.*, 2020, **5**, 1005–1016.

5 J. L. Hueso, R. Mallada and J. Santamaria, *Catal. Today*, 2023, **423**, 113927.
6 C. Faria, C. Rocha, C. Miguel, A. Rodrigues and L. M. Madeira, *Fuel*, 2025, **386**, 134269.
7 K. M. Van Geem, V. V. Galvita and G. B. Marin, *Science*, 2019, **364**, 734–735.
8 Y. Cai, J. Fu, Y. Zhou, Y.-C. Chang, Q. Min, J.-J. Zhu, Y. Lin and W. Zhu, *Nat. Commun.*, 2021, **12**, 586.
9 X. Kang, L. Li, A. Sheveleva, X. Han, J. Li, L. Liu, F. Tuna, E. J. L. McInnes, B. Han, S. Yang and M. Schröder, *Nat. Commun.*, 2020, **11**, 5464.
10 B. Peng, H. She, Z. Wei, Z. Sun, Z. Deng, Z. Sun and W. Chen, *Nat. Commun.*, 2025, **16**, 2217.
11 N. Wang, W. Jiang, J. Yang, H. Feng, Y. Zheng, S. Wang, B. Li, J. Z. X. Heng, W. C. Ong, H. R. Tan, Y.-W. Zhang, D. Wang, E. Ye and Z. Li, *Nat. Commun.*, 2024, **15**, 5913.
12 Q. Wang, T. Luo, X. Cao, Y. Gong, Y. Liu, Y. Xiao, H. Li, F. Gröbmeyer, Y.-R. Lu, T.-S. Chan, C. Ma, K. Liu, J. Fu, S. Zhang, C. Liu, Z. Lin, L. Chai, E. Cortes and M. Liu, *Nat. Commun.*, 2025, **16**, 2985.
13 C. Zhan, F. Dattila, C. Rettenmaier, A. Herzog, M. Herran, T. Wagner, F. Scholten, A. Bergmann, N. López and B. Roldan Cuenya, *Nat. Energy*, 2024, **9**, 1485–1496.
14 R. I. Masel, Z. Liu, H. Yang, J. J. Kaczur, D. Carrillo, S. Ren, D. Salvatore and C. P. Berlinguette, *Nat. Nanotechnol.*, 2021, **16**, 118–128.
15 N. Ye, K. Wang, Y. Tan, Z. Qian, H. Guo, C. Shang, Z. Lin, Q. Huang, Y. Liu, L. Li, Y. Gu, Y. Han, C. Zhou, M. Luo and S. Guo, *Nat. Synth.*, 2025, DOI: 10.1038/s44160-025-00769-9.
16 J. Gu, C. S. Hsu, L. C. Bai, H. M. Chen and X. L. Hu, *Science*, 2019, **364**, 1091–1094.
17 Z. Shang, X. T. Feng, G. Z. Chen, R. Qin and Y. H. Han, *Small*, 2023, **19**, 2304975.
18 L. Z. Liu, M. T. Li, F. Chen and H. W. Huang, *Small Struct.*, 2023, **4**, 2200188.
19 J. Zhang, W. Cai, F. X. Hu, H. Yang and B. Liu, *Chem. Sci.*, 2021, **12**, 6800–6819.
20 L. H. A. Wijewardena, W. S. Cheon, S.-H. Jeong, J. Park and H. W. Jang, *RSC Sustainability*, 2025, **3**, 2779–2805.
21 W. Chen, B. Ma and R. Zou, *Acc. Mater. Res.*, 2025, **6**, 210–220.
22 Z. Bai, Z. Zhi, X. Z. Jiang and K. H. Luo, *Ind. Eng. Chem. Res.*, 2025, **64**, 4378–4387.
23 H. Huang, K. Shen, F. Chen and Y. Li, *ACS Catal.*, 2020, **10**, 6579–6586.
24 M. Urso, X. Ju, R. Nittoor-Veedu, H. Lee, D. Zaoralová, M. Otyepka and M. Pumera, *ACS Catal.*, 2025, 11617–11663, DOI: 10.1021/acscatal.4c08027.
25 A. Madrid, A. Tolosana-Moranchel, A. García, S. Rojas, F. Bartolome, E. Pakrieva, L. Simonelli, G. Martinez, J. L. Hueso and J. Santamaria, *Chem. Eng. J.*, 2024, **498**, 155363.
26 A. Malumbres, G. Martinez, R. Mallada, J. L. Hueso, O. Bomati-Miguel and J. Santamaria, *Nanotechnology*, 2013, **24**, 325603.
27 J. L. Hueso, J. P. Espinós, A. Caballero, J. Cotrino and A. R. González-Elipe, *Carbon*, 2007, **45**, 89–96.
28 S. Díaz-Coello, G. García, M. C. Arévalo and E. Pastor, *Int. J. Hydrogen Energy*, 2019, **44**, 12576–12582.
29 A. S. Varela, M. Kroschel, N. D. Leonard, W. Ju, J. Steinberg, A. Bagger, J. Rossmeisl and P. Strasser, *ACS Energy Lett.*, 2018, **3**, 812–817.
30 A. S. Varela, N. R. Sahraie, J. Steinberg, W. Ju, H. S. Oh and P. Strasser, *Angew. Chem., Int. Ed.*, 2015, **54**, 10758–10762.
31 M. Khalil, G. T. M. Kadja, F. A. A. Nugroho, L. G. Sutanto, P. K. Jiwanti, F. F. Abdi, F. Hussin and M. K. Aroua, *Renewable Sustainable Energy Rev.*, 2024, **206**, 114869.
32 L. Wang, X. K. Liu, L. L. Cao, W. Zhang, T. Chen, Y. Lin, H. J. Wang, Y. Wang and T. Yao, *J. Phys. Chem. Lett.*, 2020, **11**, 6691–6696.
33 X. Wang, Y. Pan, H. Ning, H. Wang, D. Guo, W. Wang, Z. Yang, Q. Zhao, B. Zhang, L. Zheng, J. Zhang and M. Wu, *Appl. Catal., B*, 2020, **266**, 118630.
34 S. Díaz-Coello, D. Winkler, C. Griesser, T. Moser, J. L. Rodríguez, J. Kunze-Liebhäuser, G. García and E. Pastor, *ACS Appl. Mater. Interfaces*, 2024, **16**, 21877–21884.